



ELSEVIER

Available online at www.sciencedirect.com

ScienceDirect

Proceedings of the Combustion Institute 000 (2016) 1–8

Proceedings
of the
Combustion
Institutewww.elsevier.com/locate/proci

Modelling local extinction in Sydney swirling non-premixed flames with LES/CMC

Huangwei Zhang*, Epaminondas Mastorakos

Department of Engineering, University of Cambridge, Cambridge CB2 1PZ, United Kingdom

Received 2 December 2015; accepted 13 July 2016

Available online xxx

Abstract

The Large Eddy Simulation (LES) and three dimensional CMC (3D-CMC) model are applied to simulate the Sydney swirl-stabilized non-premixed methane flames with different levels of local extinction. The CMC model is implemented with a finite volume formulation, unstructured mesh and detailed chemistry. The statistics of velocity, mixture fraction, and major species mass fractions in both physical and mixture fraction space demonstrate very good agreement with the measured results. The level of local extinction with increased fuel bulk velocity velocities is reasonably captured. In addition, the location where flame extinction first occurs also agrees with the experimental observations. However, the statistics of the hydroxyl mass fraction, a very sensitive indicator of local extinction, have some differences from the experimental data. Budget analysis of individual terms in the CMC equation for the hydroxyl mass fraction shows that conditional convection in the CMC model has a significant role in inducing both local extinction and re-ignition events. The conditional dilatation flux contributes only when the local heat release rate is significant. © 2016 by The Combustion Institute. Published by Elsevier Inc.

Keywords: Local extinction; Re-ignition; Swirling non-premixed flames; Large eddy simulation; Conditional moment closure

1. Introduction

Flame extinction is a fundamental topic in combustion theory and is important for designing combustion systems [1]. In turbulent flames, the turbulence may induce localized and global extinction. With the first order Conditional Moment Closure (CMC) model in Large Eddy Simulation (LES), local extinction in Sandia flame F has been reasonably well predicted [2]. Recently, the CMC

model discretized in a finite volume formulation and unstructured grids was implemented [3,4] and applied to predict local extinction and blow-off in turbulent swirling non-premixed flames [5,6]. In particular, in the flames measured by Cavaliere et al. [7], the errors in the predicted blow-off air velocities, corresponding to a range of fuel flow rates, are within 25% of the experimental values [6]. Good agreement was also observed in blow-off durations and scalar evolution, compared with hydroxyl (OH) PLIF and OH* chemiluminescence images [6]. Nevertheless, a more extensive quantitative assessment of reactive scalar behaviour in flames approaching extinction, with this new

* Corresponding author. Fax: +44 1223 332662.
E-mail address: h2283@cam.ac.uk (H. Zhang).

<http://dx.doi.org/10.1016/j.proci.2016.07.051>

1540-7489 © 2016 by The Combustion Institute. Published by Elsevier Inc.

CMC implementation, needs to be made so that the prediction of the degree of local extinction is further validated. Therefore, the swirl-stabilized non-premixed flames (SMA series) with detailed Raman–Rayleigh-LIF measurements [8] from the University of Sydney and Sandia National Laboratories (one of the target flames of the Turbulent Non-premixed Flame Workshop) are selected here. Additionally, the stability limits and localized extinction levels for these flames are available [9,10]. Although LES of the Sydney swirl-stabilized flames with various combustion models has been performed [11–16], the focus on the extinction characteristics for these flames was limited.

The objectives of this study are (i) to validate the finite volume and unstructured CMC model using a flame with little extinction (SMA2) and (ii) to study the localised extinction dynamics with increased fuel flow rates (SMA3 and SMA4). Models and numerics will be introduced in Section 2, while the results and discussion are given in Section 3, followed by the conclusions.

2. Modelling

2.1. LES and CMC models

The LES equations for mass, momentum, and mixture fraction are obtained through applying low-pass Favre filtering to their instantaneous governing equations. Here, the sub-filter scale stress tensor is closed by the constant Smagorinsky model. The mixture fraction sub-filter variance ξ'' is modelled by $\xi'' = c_v \Delta^2 \nabla \xi \cdot \nabla \xi$ with $C_v = 0.1$ [17] and Δ is the filter width, specified as the cube root of the LES cell volume. The filtered scalar dissipation rate \tilde{N} includes the resolved and sub-filter parts [18]

$$\tilde{N} = \tilde{N}_{res} + \tilde{N}_{sgs}, \tag{1}$$

in which $\tilde{N}_{res} = D \nabla \xi \cdot \nabla \xi$ and $\tilde{N}_{sgs} = \frac{c_N \mu_t}{2 \bar{\rho} \Delta^2} \xi''$ with $C_N = 42$ [2]. D is the molecular diffusivity, μ_t is the turbulent viscosity and $\bar{\rho}$ is the filtered density.

The integral form of the CMC governing equations for the conditionally filtered mass fractions of α th species, i.e., $Q_\alpha \equiv \bar{Y}_\alpha | \eta$, in the LES context reads [3,4]

$$\begin{aligned} & \int_{\Omega_{CMC}} \frac{\partial Q_\alpha}{\partial t} d\Omega + \int_{\Omega_{CMC}} \nabla \cdot (\tilde{U} | \eta Q_\alpha) d\Omega \\ & = \int_{\Omega_{CMC}} Q_\alpha \nabla \cdot \tilde{U} | \eta d\Omega + \int_{\Omega_{CMC}} \tilde{N} | \eta \frac{\partial^2 Q_\alpha}{\partial^2 \eta} d\Omega \\ & + \int_{\Omega_{CMC}} \tilde{\omega}_\alpha | \eta d\Omega + \int_{\Omega_{CMC}} \nabla \cdot (D_t \nabla Q_\alpha) d\Omega, \tag{2} \end{aligned}$$

where t is time and η is the sample space variable for ξ . Ω^{CMC} denotes the CMC cell. The physical interpretations of terms T_0 to T_5 in Eq. (2) are unsteadiness, convection, dilatation, micromixing, chemistry, and sub-filter diffusion, respectively. The quantities $\tilde{U} | \eta$, $\tilde{N} | \eta$, and $\tilde{\omega}_\alpha | \eta$ are the conditionally filtered velocity, scalar dissipation rate, and reaction rates of the α th species, respectively. D_t is the sub-filter diffusivity, and given by $D_t = \mu_t / \bar{\rho} Sc_t$ with the turbulent Schmidt number $Sc_t = 0.4$ [19], which may lead to high dissipation from sub-filter contribution to scalar behaviours but gives reasonable results for the investigated flames (e.g., shown later in Fig. 3) and for other swirling flames in the same burner [13,16].

The assumption $\tilde{U} | \eta \approx \tilde{U}$ is adopted for Eq. (2). For $\tilde{N} | \eta$, the Amplitude Mapping Closure (AMC) model [20] is applied, i.e., $\tilde{N} | \eta = N_0 G(\eta)$, where $G(\eta) = \exp(-2[\text{erf}^{-1}(2\eta - 1)]^2)$. The variable N_0 is the scalar dissipation at $\eta = 0.5$, and calculated from $N_0 = \tilde{N} / \int_0^1 \tilde{P}(\eta) G(\eta) d\eta$. The filtered scalar dissipation rate \tilde{N} is calculated with Eq. (1). The Filtered Density Function (PDF) $\tilde{P}(\eta)$ is calculated from a β -function with ξ and ξ'' . The first order CMC model is used such that $\tilde{\omega}_\alpha | \eta = \omega_\alpha(Q_1, \dots, Q_n, Q_T)$. Here n is the species number and $Q_T \equiv T | \eta$ represents the conditional temperature. The filtered variable \tilde{f} is calculated from the conditional value $\tilde{f} | \eta$ through $\tilde{f} = \int_0^1 \tilde{f} \tilde{P}(\eta) d\eta$.

Assuming that all the conditional variables $\tilde{f} | \eta$ and the derivative in η -space, $\partial^2 Q_\alpha / \partial^2 \eta$, are constant within one CMC cell, Eq. (2) can be discretized with the finite volume method in physical space as follows [3]:

$$\begin{aligned} & \frac{\partial Q_\alpha}{\partial t} + \frac{1}{V_{CMC}} \sum_{m=1}^{n_f} (Q_\alpha \tilde{U} | \eta \cdot \mathbf{n})_m \Delta S_m \\ & = \frac{1}{V_{CMC}} Q_\alpha \sum_{m=1}^{n_f} (\tilde{U} | \eta \cdot \mathbf{n})_m \Delta S_m + \tilde{N} | \eta \frac{\partial^2 Q_\alpha}{\partial^2 \eta} \\ & + \tilde{\omega}_\alpha | \eta + \frac{1}{V_{CMC}} \sum_{m=1}^{n_f} (D_t \nabla Q_\alpha \cdot \mathbf{n})_m \Delta S_m, \tag{3} \end{aligned}$$

where n_f and V_{CMC} are, respectively, the number of faces and volume of a CMC cell, \mathbf{n} is the unit normal face vector and ΔS is the face area.

2.2. Flame information and numerical implementation

The Sydney swirl burner comprises a bluff body with diameter $D_b = 0.05$ m [8–10]. Fuel is injected

Table 1
Flow conditions for the simulated cases.

Cases	U_S (m/s)	W_S (m/s)	U_j (m/s)	$U_j / U_{j,SL}$ (%)	\dot{W} (kW)	Re_j
SMA2	16.3	25.9	66.3	31	11.5	15,400
SMA3			132.6	62	23.0	30,800
SMA4			225.0	104	39.0	52,300

through a jet (diameter $D_j=0.0036$ m, located in the bluff body centre) with bulk velocity U_j . Here only the SMA flame series with fuel being Compressed Natural Gas (CNG)/air (1:2 vol.) will be studied with the CNG replaced by pure methane (CH_4) in the computations. The stoichiometric mixture fraction ξ_{st} is 0.25. The primary swirling air with axial bulk velocity U_s and swirl bulk velocity W_s is fed through the annular gap ($D_a=0.06$ m), concentrically surrounding the bluff body. Here, U_s and W_s are estimated from the axial and tangential air mass flow rates, respectively. The secondary (co-flow) axial bulk velocity U_e is 20 m/s with 2% turbulence intensity.

Three cases are selected for LES, i.e., SMA2, SMA3, and SMA4 (flow conditions in Table 1). The velocity, mixture fraction and compositions of SMA2 and SMA3 were measured [8]. Nevertheless, SMA4 has no measurements and is used to examine the CMC model for extinction. These cases have the same primary air inlet velocities, $U_S=16.3$ m/s and $W_S=25.9$ m/s, and therefore the same swirl number $S_N=W_S/U_S=1.59$. However, from SMA2 to SMA4, U_j is progressively increased (therefore increased thermal power \dot{W} and fuel jet Reynolds number Re_j), i.e., $U_j=66.3$ m/s, 132.6 m/s to 225 m/s, respectively, corresponding to 31%, 63% and 104% of the stability limit (the critical jet velocity $U_{j,SL}=216$ m/s [9]) for $U_S=16.3$ m/s and $W_S=25.9$ m/s. Note that $U_{j,SL}$ corresponds to the critical jet velocity with which the earliest occurrence of *visible* localized extinction at the base near the bluff body is observed experimentally [9].

The cylindrical LES computational domain starts at the burner exit plane and its scale is $6D_b \times 3D_b \times 2\pi$ in the longitudinal, radial and azimuthal directions, respectively. The coordinate origin lies at the center of the jet exit. x is the axial coordinate while y and z are the spanwise ones. Approximately 8,400,000 tetrahedral LES cells are generated. The domain extent for CMC in physical space is identical to the LES one. About 120,000 polyhedral CMC cells (on average one CMC cell consists of 70 LES cells) are constructed from LES cells to discretize the domain, through determining the CMC faces from LES ones whose owner and neighbour LES cells have different host CMC nodes [3,4]. The mixture fraction space is discretized by 51 nodes.

For the LES, the axial velocity at the fuel jet and the axial and swirl velocities at the swirling primary air inlet are specified using the one-seventh power

law based on their individual bulk velocities [21]. The inlet synthesized turbulence method is used [22], matching the available measurements. Zero radial velocity is assumed for the primary air inlet. At the side and outflow boundaries, zero gradient conditions for the velocities are assumed, while non-slip condition is enforced for the bluff-body wall. Zero pressure gradient is enforced for all the outlets and the bluff-body wall. The mixture fraction is unity at the fuel inlet, zero for the air inlets, and has zero gradient at the side and outflow boundaries. For the CMC domain, the inert mixing Q_α solutions are assumed at all inlets. For the bluff body wall, side and outlet boundaries, zero gradient conditions for Q_α are applied.

In η -space, at oxidizer boundary $\eta=0$, the mass fractions of O_2 and N_2 are 23.3% and 76.7%, respectively, while at fuel boundary $\eta=1$, those of O_2 , N_2 and CH_4 are 18.2%, 59.9%, and 21.9%, respectively. The temperatures for both boundaries are 298 K. Q_α predicted using a stand-alone 0D-CMC (Eq. 2 without T_1 , T_2 , and T_5) solver with the above boundary conditions and constant scalar dissipation rate $N_0=150$ 1/s is used for initializing all the CMC cells.

The CMC solver is interfaced with the OpenFOAM® LES solver [3]. For LES, the numerics are identical to what are used previously [5]. A second-order backward scheme is applied for time discretization. A central differencing scheme is used for diffusion and convection terms in the momentum equation, while the convection term in the mixture fraction equation is discretized with a TVD scheme. The time steps for SMA2, SMA3 and SMA4 are 2×10^{-6} s, 1×10^{-6} s and 0.6×10^{-6} s, respectively, which ensures that the maximum CFL number is less than 0.5. An operator splitting method is applied for the discretised CMC equations, Eq. (3). For terms in physical space (T_1^* , T_2^* and T_5^*), a first order Euler time scheme is applied. First-order upwind and second-order central differencing schemes are used for T_1^* and T_5^* . TDMA is applied in η -space for solving T_3 , while the stiff ODE solver VODPK [23] is used for T_4 . The ARM2 mechanism (19 species and 15 reactions) [24] is used. For the fuel composition in the SMA series, extinction occurs at a scalar dissipation $N_0=298$ 1/s, determined from 0D-CMC calculations (i.e. the corresponding scalar dissipation at stoichiometry calculated from AMC model is $N|\xi_{st}=188.8$ 1/s). These values are close to those ($N_0=306$ 1/s and $N|\xi_{st}=193.8$ 1/s) from GRI

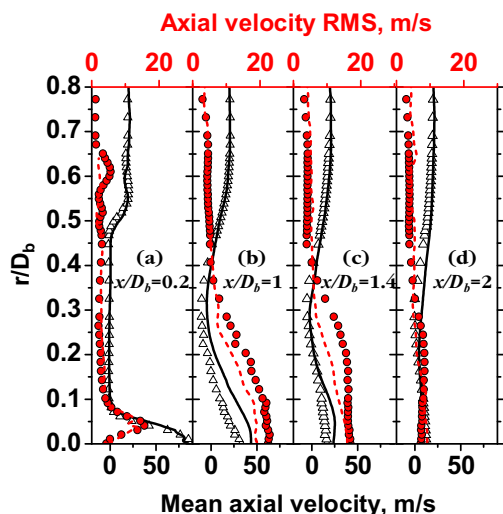


Fig. 1. Radial profiles of SMA2 axial velocity statistics at the indicated streamwise locations. Symbols: experiments [9]; lines: simulations. Triangles and solid lines: mean; circles and dashed lines: RMS.

3.0 mechanism [25]. On-the-fly bi-directional data exchange between two solvers is executed [4–6]. 480 processors were used for the current computations and 20 flow-through times τ (estimated as $\tau = L_{\xi}/U_j$, where L_{ξ} is the centreline location of ξ_{st} , 0.12 m based on the experiments for SMA2 and SMA3 [8]) were computed. The statistics for SMA2 and SMA3 were compiled between $10\tau \leq t \leq 20\tau$ so that the LES and CMC fields are fully developed.

3. Results and discussion

3.1. SMA2

Comparisons of SMA2 axial velocity mean and Root Mean Square (RMS) from LES/3D-CMC and experiments [9] are made in Fig. 1. The mean axial velocity is reasonably well predicted for all the presented locations. The least satisfactory position is $x/D_b = 1.0$, where the computational mean is slightly over-predicted for $r/D_b < 0.3$. Some differences exist for the RMS. At $x/D_b = 1.0$ and 1.4, the LES underpredicts the fluctuations close to the fuel jet, but the trends of its radial distributions are still reasonably captured. The SMA2 swirl velocity statistics are shown in Fig. 2. Besides the swirling motion from the primary air inlet, a strong rotation around the fuel jet base was observed experimentally [9] and this can be seen in Fig. 2a as the double-humped profiles of swirl velocity. However, in the current computations the latter is slightly under-predicted (see $x/D_b = 0.2$ and 1.0 in Fig. 2). This under-prediction was seen as well in LES/FDF of SMA1 case [12] and this may be

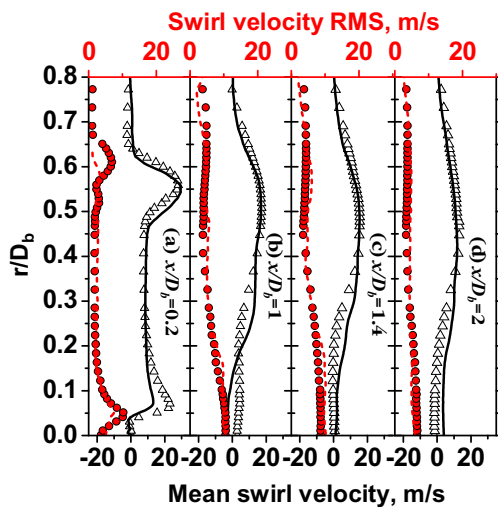


Fig. 2. Radial profiles of SMA2 swirl velocity statistics at the indicated streamwise locations. Legend as in Fig. 1.

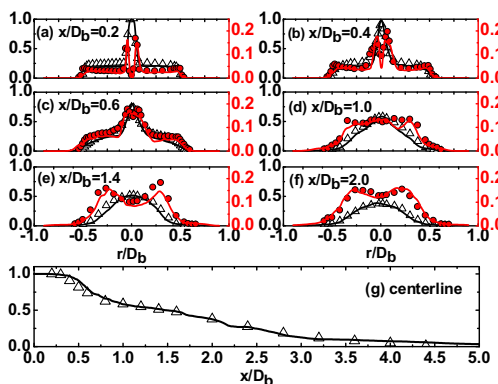


Fig. 3. (a–f) Radial and (g) centerline profiles of SMA2 mixture fraction mean (left ordinate) and RMS (right ordinate). Legend as in Fig. 1. Experimental data from Ref. [8].

affected by the inaccuracy of turbulent boundary specifications at both jet exit and annular primary air inlet. The swirl velocity RMS is well reproduced in the LES, as presented in Fig. 2.

Figure 3a–f show radial profiles of mixture fraction statistics for SMA2, while Fig. 3g shows the centreline decay of the mean. Both mean and RMS of mixture fraction demonstrate excellent agreement with the measured data for all the presented streamwise locations and the centreline. The mean mixture fraction is slightly lower than the experimental data for $0.1 < |r|/D_b < 0.4$ at the upstream locations, i.e. $x/D_b = 0.2$ and 0.4 in Fig. 3a and b. In addition, based on Fig. 3g, the centreline flame length is around 0.125 m from the LES, close to the experimental value $L_{\xi} = 0.12$ m [8].

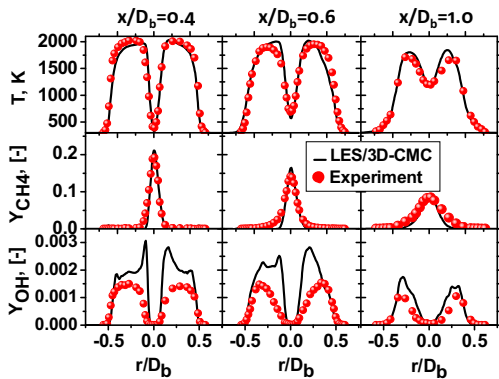


Fig. 4. Radial profiles of mean temperature (upper row), CH₄ (middle row) and OH (bottom row) mass fractions from SMA2. Experimental data from Ref. [8].

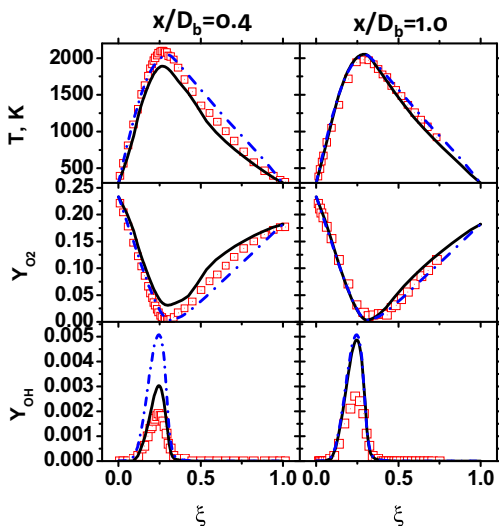


Fig. 5. Time averaged conditional temperature, O₂ and OH mass fractions from SMA2. Symbols: measurements [8]; solid lines: LES/3D-CMC; dashed lines: 0D-CMC.

Radial distributions of the time averaged temperature, \tilde{T} , CH₄ and OH mass fractions, $\langle \tilde{Y}_{CH_4} \rangle$ and $\langle \tilde{Y}_{OH} \rangle$, are presented in Fig. 4. The fields of \tilde{T} and $\langle \tilde{Y}_{CH_4} \rangle$ are correctly predicted, including the peak values and their locations. Nevertheless, at $x/D_b = 0.4$ and 0.6 , the computed $\langle \tilde{Y}_{OH} \rangle$ is considerably higher than the measured one, although downstream (see $x/D_b = 1.0$) the agreement is improved. This difference was also observed in LES/FGM modelling of SMA2 with GRI 3.0 mechanism [14] and FDF modelling with GRI 2.11 [15]. Figure 5 shows the mean conditional temperature, $\langle \tilde{T} | \eta \rangle$, O₂ and OH mass fractions, $\langle \tilde{Y}_{O_2} | \eta \rangle$ and $\langle \tilde{Y}_{OH} | \eta \rangle$, at two streamwise locations. The conditional means were calculated at the same

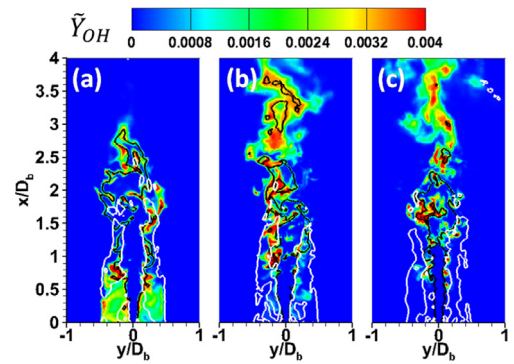


Fig. 6. Contours of \tilde{Y}_{OH} from (a) SMA2, (b) SMA3 and (c) SMA4. Black lines: stoichiometric mixture fraction; white lines: zero axial velocity.

radial locations (e.g., $|r| < 0.16D_b$ for SMA2) as the measurements. The fully burning profiles from 0D-CMC calculations are also shown. At $x/D_b = 0.4$, the computed $\langle \tilde{T} | \eta \rangle$ and $\langle \tilde{Y}_{O_2} | \eta \rangle$ are respectively lower and higher than the measured ones, indicating that the considerable transient flame structure may deviate from the near-equilibrium state. However, at $x/D_b = 1.0$, good agreement is shown for both $\langle \tilde{T} | \eta \rangle$ and $\langle \tilde{Y}_{O_2} | \eta \rangle$. For $\langle \tilde{Y}_{OH} | \eta \rangle$, however, its magnitude close to $\xi_{st} = 0.25$ is over-predicted at both locations. This may lead to the higher mean OH mass fraction shown in Fig. 4. Over-predictions of OH mass fraction were also observed, e.g., from LES/FGM [14] and LES/FDF [15] of SMA2, LES/FDF [26], LES/CMC [2], and RANS/PDF (Reynolds Averaged Navier–Stokes with Probability Density Function model) [27] of Sandia flames. It was attributed to the chemical kinetics used and/or the response of OH to local scalar dissipation fields. In the present sub-filtered CMC model, this may also result from the fact that $\langle \tilde{Y}_{OH} | \eta \rangle$ shows a strong sensitivity to the instantaneous variations of scalar dissipation rate estimated with AMC model or conditional numerical fluxes (e.g. convection) and hence cannot sustain itself at an intermediate level for a long time [2,5].

3.2. SMA3 and SMA4

Contours of filtered OH mass fractions \tilde{Y}_{OH} are presented in Fig. 6. For $x/D_b < 2.0$, the iso-lines of ξ_{st} are close to the Recirculation Zone (RZ) inner boundaries surrounding the fuel jet and the length and shape of the RZ do not change qualitatively from SMA2 to SMA4. For SMA2, \tilde{Y}_{OH} is high along the whole iso-lines of stoichiometric mixture fraction, indicating that there is little local extinction in SMA2. This agrees well with the experiment [8]. In addition, considerable OH is also observable in the upstream part of the RZ, which is consistent

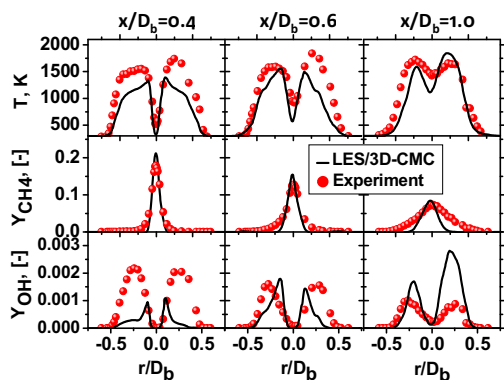


Fig. 7. Radial profiles of mean temperature (upper row), CH₄ (middle row) and OH (bottom row) mass fractions from SMA3. Experimental data from Ref. [8]. Statistics compiled with 10 flow-through times after first 10 flow-through times to eliminate the initial field effects.

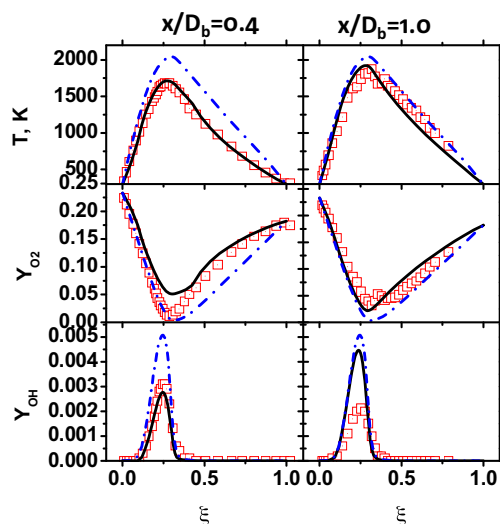


Fig. 8. Mean conditional temperature, O₂ and OH mass fractions from SMA3. Legend as in Fig. 5.

with the local mixture fraction value being close to ξ_{st} (Fig. 3). When the fuel jet velocity is doubled in SMA3, Y_{OH} becomes much lower in the upstream part of the RZ and the flame has been lifted off the bluff body surface. In addition, along the right branch of ξ_{st} iso-lines at $1.0 < x/D_b < 2.0$, \tilde{Y}_{OH} is also reduced (Fig. 6b). Beyond $x/D_b = 2.5$, OH pockets are transported from upstream due to the increased local velocity and also turbulence compared to SMA2. For SMA4 in Fig. 6c, the flame is lifted more and the flame becomes more fragmented than SMA3, which implies that there are more severe localised extinctions occurring. The current LES/3D-CMC reasonably well predicts the varying local extinction extent with increasing fuel jet velocity. Also, the local extinction first appears at the flame base, consistent with experiment [8]. However, the computations predict local extinction with a smaller fuel jet velocity (SMA3), which still corresponds to a fully burning flame in the experiments and actually the operating conditions of SMA4 slightly exceed the stability limits $U_{i,SL} = 216$ m/s, beyond which onset of instantaneous localised extinction is visibly found [8].

Radial profiles of \tilde{T} , \tilde{Y}_{CH_4} and \tilde{Y}_{OH} , for SMA3 are shown in Fig. 7. \tilde{Y}_{CH_4} is predicted well, while \tilde{T} is under-predicted in the RZ at $x/D_b = 0.4$ and 0.6. Similar to the SMA2 results in Fig. 4, discrepancies exist between the computed \tilde{Y}_{OH} and the measurements. Additionally, the asymmetry of the computed reactive scalars in Fig. 7 may be caused by a not sufficiently long period (i.e., 10τ) for the statistics collection in SMA3 case. Figure 8 presents $\tilde{T}|\eta$, $\tilde{Y}_{O_2}|\eta$ and $\tilde{Y}_{OH}|\eta$ from SMA3. At $x/D_b = 0.4$, good agreement of calculated $\tilde{T}|\eta$ and $\tilde{Y}_{OH}|\eta$ with the experimental results is obtained. Therefore, the under-prediction of \tilde{Y}_{OH} at $x/D_b = 0.4$ in SMA3 probably results from the lower

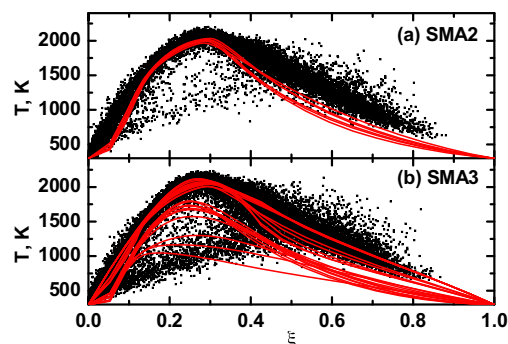


Fig. 9. Conditional temperature at $x/D_b = 1$ and $r/D_b < 0.6$ at different time instants from (a) SMA2 and (b) SMA3. The scatter plot is from the experiment [8].

computed local mixture fraction field [3], which is also a source for the OH deviation in the current simulations. In the LES results, higher $\tilde{Y}_{O_2}|\eta$ exists near $\xi_{st} = 0.25$, which indicates smaller reactivity. At $x/D_b = 1.0$, $\tilde{T}|\eta$ and $\tilde{Y}_{O_2}|\eta$ are correctly predicted, however, $\tilde{Y}_{OH}|\eta$ is again over-calculated, due to the under-prediction of localised extinction. Compared to the SMA2 counterparts in Fig. 5, experimentally, SMA3 demonstrates stronger indications for its flame structures deviating from the fully reactive state, such as lower temperature and higher oxidizer concentration at stoichiometry.

The instantaneous evolutions of conditionally filtered temperature $\tilde{T}|\eta$ from SMA2 and SMA3 extracted from the CMC cells located at $x/D_b = 1$ and $r/D_b < 0.6$ are plotted in Fig. 9. In the SMA2 case, $\tilde{T}|\eta$ has comparatively small variations which

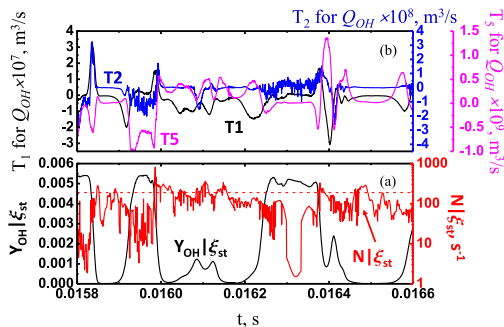


Fig. 10. Time evolutions of conditional (a) OH mass fraction, scalar dissipation rate, and (b) convection, dilatation and sub-filter diffusion fluxes at $\xi_{st} = 0.25$. Results extracted from one CMC cell at $x/D_b = 0.8$, $y/D_b = 0.08$ and $z/D_b = 0$ in SMA4. The dashed line in (a) denotes the critical extinction value from 0D-CMC, $N|\xi_{st} = 188.8 \text{ 1/s}$.

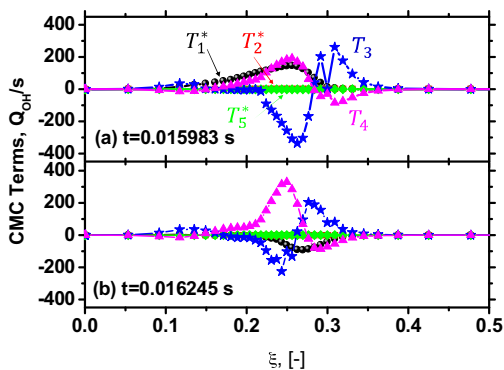


Fig. 11. Budget analysis of CMC terms for the conditional OH mass fraction. Results extracted from the same CMC cell as in Fig. 10.

are consistent with the experimental results. However, in the SMA3 case, considerable variations of $\overline{T|\eta}$ can be seen and the $T|\eta$ at ξ_{st} can be as low as about 1000 K, approaching an inert mixing state. These variations are also present in the experimental data with the large scatter shown in Fig. 9b.

Localised extinctions in SMA4 presented in Fig. 6c are further analysed in Figs. 10 and 11. The results in Fig. 10 are extracted from a CMC cell located at $x/D_b = 0.8$, $y/D_b = 0.08$ and $z/D_b = 0$. Figure 10a shows the time evolutions of $\overline{Y_{OH}|\xi_{st}}$ and $\overline{N|\xi_{st}}$. $\overline{Y_{OH}|\xi_{st}}$ alternately changes between 0 and 0.005, which indicates the frequent occurrence of local extinction (e.g., $t = 0.016$ s) and re-ignition (e.g., $t = 0.01625$ s). It has been accepted that the scalar dissipation rate plays a key role in modelling local extinction with the CMC model [2,5,6] and in the current results, the durations with low $\overline{Y_{OH}|\xi_{st}}$ (e.g., between $t = 0.016$ and 0.0162 s) and therefore occurrence of localised extinction are indeed ex-

posed to the scalar dissipation rates close to the critical extinction value from 0D-CMC calculations. The evolution of the convection, dilatation and sub-filter diffusion fluxes, i.e., CMC terms in physical space ($V_{CMC}T_1^*$, $V_{CMC}T_2^*$ and $V_{CMC}T_5^*$ in Eq. 3), for the OH are plotted in Fig. 10b. Their respective discretised forms within finite volume framework can be found in Eq. (3). It can be seen that the magnitude of $V_{CMC}T_5^*$ is negligibly small, compared to that of $V_{CMC}T_1^*$ and $V_{CMC}T_2^*$, consistent with the finding from LES/CMC of Sandia flame [28]. Additionally, the contribution from $V_{CMC}T_2^*$ is also lower than that from $V_{CMC}T_1^*$ and when localised extinction happens with very low OH, $V_{CMC}T_2^*$ is very close to zero, which can be confirmed by its discretised equation in Eq. (3). When the CMC cell is fully reactive, dilatation flux demonstrates the pronounced low-frequency fluctuations, probably following the variations of volume flux $\overline{U|\eta} \cdot \mathbf{n}\Delta S$ at the CMC faces. Also, it can be negative or positive contribution to local $\overline{Y_{OH}|\xi_{st}}$. The evolution of convection flux is interesting. Clearly, there are corresponding positive (efflux) or negative (influx) contributions when local extinction or re-ignition occurs, shown in Fig. 10b. Actually this relation is not limited to this analysed CMC cell, and this implies that the convection flux $V_{CMC}T_1^*$ can also result in or facilitate local extinction, besides re-ignition. The latter has been pointed out in Refs. [2,5,29] with the CMC modelling.

A budget analysis of the individual CMC terms from Eq. (3) with respect to $\overline{Y_{OH}|\eta}$ is made in Fig. 11 for both localised extinction ($t = 0.015983$ s in Fig. 10) and re-ignition ($t = 0.016245$ s) events. Results in Fig. 11 are from the same CMC cell as that in Fig. 10. When extinction happens, T_3 shows significant negative contribution. The magnitude of T_1^* is comparable with that of T_3 , and the former tends to reduce $\overline{Y_{OH}|\eta}$. T_4 is still finite since complete extinction has not been reached. However, during the re-ignition in Fig. 11b, the convection flux T_1^* has negative values, indicating the influx of $\overline{Y_{OH}|\eta}$ from the neighboring cells. Therefore, convection constitutes one of the reasons to re-ignite the flame due to the interaction between neighbouring CMC cells in physical space. However, it is still not clear if the re-ignition can also occur in η -space with cold fuel ($\eta = 0$) and oxidizer ($\eta = 1$) boundaries. Stand-alone 0D-CMC calculation with instantaneous $\overline{N|\eta}$ from an extinguished cell in the 3D-CMC simulation [2] showed that this cell cannot become re-burning without physical transport unless the scalar dissipation falls to low values for a long period. In addition, the magnitudes from T_2^* and T_5^* are negligible for both instants in Fig. 11, consistent with the findings from Fig. 10. Therefore, the conditional convection plays a significant role in onset of both local extinction and re-ignition.

4. Conclusions

The LES/3D-CMC model with detailed chemistry is used to simulate the Sydney swirling non-premixed flames with different levels of localised extinction. The current simulations predict reasonably well the statistics of velocity, mixture fraction, and major species mass fraction in physical and mixture fraction space. However, discrepancies exist for the hydroxyl mass fraction, possibly due to its response to the scalar dissipation rate and the resolved mixture fraction. The LES/3D-CMC also captures the level of local extinction in three cases with progressively increased fuel jet velocities. Additionally, the location where local extinction first occurs also agrees with experiment. The contributions from each term in the CMC equation for OH mass fraction are analysed and it is found that both local extinction and re-ignition are affected by the convective flux, while the dilatation has a finite contribution only when the local flame structure is far from extinction.

Acknowledgement

This work used the ARCHER UK National Supercomputing Service (<http://www.archer.ac.uk>).

References

- [1] C.K. Law, *Combustion Physics*, Cambridge University Press, New York, 2006, p. 303.
- [2] A. Garmory, E. Mastorakos, *Proc. Combust. Inst.* 33 (2011) 1673–1680.
- [3] H. Zhang, *Extinction in Turbulent Swirling Non-premixed Flames. Ph.D. Thesis*, University of Cambridge, Cambridge, United Kingdom, 2015. Available at <https://www.repository.cam.ac.uk/handle/1810/254974>.
- [4] A. Garmory, E. Mastorakos, *Proc. Combust. Inst.* 35 (2015) 1207–1214.
- [5] H. Zhang, A. Garmory, D.E. Cavaliere, E. Mastorakos, *Proc. Combust. Inst.* 35 (2015) 1167–1174.
- [6] H. Zhang, E. Mastorakos, *Flow Turbul. Combust.* 96 (2016) 863–889.
- [7] D. Cavaliere, J. Kariuki, E. Mastorakos, *Flow Turbul. Combust.* 91 (2013) 347–372.
- [8] A.R. Masri, P.A.M. Kalt, R.S. Barlow, *Combust. Flame* 137 (2004) 1–37.
- [9] Y.M. Al-Abdeli, A.R. Masri, *Combust. Theory Model.* 7 (2003) 731–766.
- [10] A.R. Masri, P.A.M. Kalt, Y.M. Al-Abdeli, R.S. Barlow, *Combust. Theor. Model.* 11 (2007) 653–673.
- [11] H. El-Asrag, S. Menon, *Proc. Combust. Inst.* 31 (2) (2007) 1747–1754.
- [12] S. James, J. Zhu, M. Anand, *Proc. Combust. Inst.* 31 (2) (2007) 1737–1745.
- [13] A. Kempf, W. Malalasekera, K. Ranga-Dinesh, O. Stein, *Flow Turbul. Combust.* 81 (4) (2008) 523–561.
- [14] C. Olbricht, A. Ketelheun, F. Hahn, J. Janicka, *Flow Turbul. Combust.* 85 (3–4) (2010) 513–547.
- [15] N. Ansari, P. Piscueneri, P. Strakey, P. Givi, *AIAA J.* 50 (11) (2012) 2476–2482.
- [16] O. Stein, A. Kempf, *Proc. Combust. Inst.* 31 (2) (2007) 1755–1763.
- [17] C.D. Pierce, P. Moin, *Phys. Fluids* 10 (1998) 3041–3044.
- [18] C. Pera, J. Réveillon, L. Vervisch, P. Domingo, *Combust. Flame* 146 (2006) 635–648.
- [19] H. Pitsch, H. Steiner, *Phys. Fluids* 12 (10) (2000) 2541–2554.
- [20] O.E. Brien, T.L. Jiang, *Phys. Fluids* 3 (1991) 3121–3123.
- [21] A.R. Masri, S.B. Pope, B.B. Dally, *Proc. Combust. Inst.* 28 (1) (2000) 123–131.
- [22] N. Kornev, E. Hassel, *Commun. Numer. Meth. Eng.* 23 (1) (2007) 35–43.
- [23] P.N. Brown, A.C. Hindmarsh, *J. Comput. Appl. Math.* 31 (1989) 40–91.
- [24] C. Sung, C. Law, J.-Y. Chen, *Symp. (Int.) Combust.* 27 (1998) 295–304.
- [25] G.P. Smith, D.M. Golden, M. Frenklach, et al., GRI-MECH 3.0, available at <http://combustion.berkeley.edu/gri-mech/version30/text30.html>.
- [26] W. Jones, V. Prasad, *Combust. Flame* 157 (9) (2010) 1621–1636.
- [27] J. Xu, S.B. Pope, *Combust. Flame* 123 (2000) 281–307.
- [28] A. Garmory, E. Mastorakos, *Int. J. Heat Fluid Fl.* 39 (2013) 53–63.
- [29] S. Navarro-Martinez, A. Kronenburg, *Flow Turbul. Combust.* 87 (2011) 377–406.